FIRST LIGHT CURVE OBSERVATIONS FROM GSOC-OPERATED SMARTNET TELESCOPE STATIONS WITH AN SCMOS CAMERA

Yonathan Ascanio Hecker, Johannes Herzog, and Hauke Fiedler

German Aerospace Center, Space Operations and Astronaut Training, Münchener Straße 20, 82234 Weßling, Germany, Email: yonathan.ascaniohecker@dlr.de

ABSTRACT

SMARTnet is a network of sensor operators that observe resident space objects, both satellites and space debris, and exchanges the collected data for further processing by each member. The German Space Operations Center is remotely operating three passive-optical robotic telescope stations on the southern hemisphere as part of SMARTnet and has recently switched one of the telescopes' cameras from a charge-coupled device (CCD) to a scientific complementary metal-oxide-semiconductor (sCMOS) camera to obtain high-cadence light curves of resident space objects.

In this paper, we present the first light curve observations of resident space objects obtained with the 50-cm telescope SMART-03-A-ELSA at the SMARTnet telescope station in Chile using an FLI Kepler4040 sCMOS camera. The system is controlled by our own telescope station control software, SMARTies, demonstrating its capability and flexibility in observation modes. We also compare different methods of obtaining brightness estimates, namely fitting a Gaussian and Moffat profile to the brightness distribution, and aperture summation with the aperture informed by the former method.

The two targets selected were 2002–040B (NORAD 27509), a satellite in a graveyard orbit, and 2004–050B (NORAD 28546), an upper stage rocket body in geostationary transfer orbit. We analyse the newly obtained light curves for signs of periodicity, extract observable periods where appropriate, and compare these to previously published values.

From our uncorrected data, we obtain a synodic rotational period of (68.0 ± 5.5) s for 2004–050B. Further, we show that the Moffat profile is not always a good model for resident space objects, especially towards the edges of the field of view, and that the integral over the Gaussian distribution and aperture summation result in similar results for strong signals, even under these somewhat difficult circumstances.

Keywords: Light curve; SMARTnet; resident space objects.

1. INTRODUCTION

The cataloguing of orbital data for resident space objects is a crucial task for space traffic management, including for tasks such as performing collision avoidance manoeuvres. Due to the increase in resident space objects, these manoeuvres are not a solution, but rather an action born from necessity, whereas the solution involves lowering the amount and fraction of space debris among the resident space object population, such as through active debris removal. Some of the most known sources of orbital information about resident space objects include space-track.org[1], a catalogue maintained by the Unites States 18th Space Defense Squadron, and the High Accuracy Catalog, also known as the Special Perturbation Catalog, maintained by the Space Surveillance Network.

Light curves – time series data of the observed brightness of an object – are the natural next step from passive optical observations of resident space objects. They can carry information about the attitude and rotational properties of the resident space object in question, as has been shown in, e.g., [2, 3, 4]. Some work has also gone into shape estimation and reconstruction using various methods, including, but not restricted to, AI [5, 6]. There have also been efforts to compile databases of light curves, such as the Space Debris Light Curve Database [7] or the light curve database of the Astronomical Institute of the University of Bern [8].

In this paper, we present the first light curve observations obtained with a passive-optical telescope system owned and operated by the German Space Operations Center (GSOC), with different methods of brightness estimation and subsequent period analysis. We will give an overview of the telescope system used and of the observation target in Sections 2 and 3, respectively. Section 4 contains the methods employed for light curve extraction, with the results presented in Section 5. Finally, we will summarise our findings in Section 6.

Proc. 9th European Conference on Space Debris, Bonn, Germany, 1–4 April 2025, published by the ESA Space Debris Office
Editors: S. Lemmens, T. Flohrer & F. Schmitz, (http://conference.sdo.esoc.esa.int, April 2025)

2. INSTRUMENTATION

The Small Aperture Robotic Telescope Network (SMARTnet) [9, 10] is a network of telescope station operators dedicated to observations of resident space objects. In order to maximise the scientific or product output for all partners, all data obtained is shared between all partners, such that obtaining orbital information or light curve measurements becomes more complete and simultaneously affordable for every party involved.

The GSOC-operated telescope station SMART-03-ELSA is located at El Sauce, Chile, and has been in continuous operation since February 2024. It consists of two telescopes on a single mount. One telescope is a PlaneWave CDK20, which has a primary mirror diameter of $508\,\mathrm{mm}$ and a focal length of $3454\,\mathrm{mm}$, resulting in a field of view of about $0.61° \times 0.61°$. The second telescope is an ASA 10N with a primary mirror of $254\,\mathrm{mm}$ diameter and a focal length of $902\,\mathrm{mm}$. [11]
As alluded to in [12], the 50-cm telescope was upgraded to feature a Finger Lakes Instrumentation (FLI) Kepler4040 scientific complementary metal-oxide-semiconductor (sCMOS) camera in January of 2025. It enables much faster image readout than the previously used FLI ProLine 16803 charge-coupled device (CCD) camera, both of which share the setup of 4096×4096 pixels of size $9\,\mu\mathrm{m}$. More information about the system can be found in [11].

The Kepler4040 uses two distinct 12-bit readout channels with different gains (about $0.8\,\mathrm{e}^-/\mathrm{ADU}$ (electrons per analogue-to-digital unit) and $17.8\,\mathrm{e}^-/\mathrm{ADU}$, according to the manufacturer[1]) when obtaining an image. These can be combined to a single pseudo-16-bit frame with a high dynamic range and values reaching up to the 16 bit ceiling of 65 535, but not every value above ~ 4000 can be populated from this data. From a photometric standpoint, these merged frames offer no apparent value to the authors over the underlying 12-bit images, so they will not be used in this paper. Instead, we will be treating both gain channels as separately observed frames, resulting in their individual light curves.

3. LIGHT CURVE OBSERVATIONS

The observations presented here target two objects. The first is 2002-040B (NORAD 27509), also known as Meteosat 8 or MSG-1. It is currently in a graveyard orbit, specifically with a semi-major axis of around $42\,842\,\mathrm{km}$, an inclination of around $10.3°$, and an eccentricity of roughly 0.0016, according to the space-track.org catalogue [1]. The second is 2004-050B (NORAD 2828546), a Delta IV upper stage rocket body on an orbit with a semi-major axis of around $34\,104\,\mathrm{km}$, an inclination of around $16.5°$, and an eccentricity of roughly 0.2588, according to space-track.org [1].

All observations were obtained using the SMARTnet Instrument Enhancing Software (SMARTies) [13]. The observations for 2002–040B were performed on February 12th, 2025, with the Kepler4040 in several batches of ten consecutive full frames, each with an exposure time of $4\,\mathrm{s}$. The earliest exposure began at 2025-02-07:36:14 UTC, while the last exposure began at 08:07:52 UTC. As it turns out, taking full frames in the fully automated mode was a good choice, as the target object consistently ended up near the edge of the field of view. The reason for this is under investigation, although one explanation may be insufficiently accurate TLE data used for the orbit propagation and subsequently for tracking. The observations for 2004–050B were performed outside the fully automated mode on March 6th, 2025, as a small batch of 30 consecutive subframes of 150×150 pixels with an exposure time of $5.4\,\mathrm{s}$ each. Again, the target had been tracked offset from the sensor centre, albeit with a lower offset than seen in the observations of 2002–040B. These latter observations were part of a validation campaign for the proper functionality of SMARTies, leading to the short observation period.

4. LIGHT CURVE EXTRACTION

To get a grasp on the applicability of several methods, we used three methods of extracting the brightness information.

The first method is related to [14]. There, a model is fit to the obtained data, and the model parameters are used as estimators for the underlying brightness. In this case, we assume that the brightness within each pixel is the sum of the camera background (i.e., bias and dark signal), N, a sky background constant across the region used for the fit, B, and the source intensity, S:

$$I(x, y) = N(x, y) + B + S(x, y) \quad . \tag{1}$$

The distinction to the work of [14] is that in our case, the detector signal is a 2-dimensional array instead of a 1-dimensional one; we will assume for this paper without proof that the generalisation of the concept to two dimensions holds. We further assume for this method that the signal S is described by a scaled 2-dimensional Gaussian distribution,

[1] Interestingly, as will be seen in section 5, the gain ratio provided by the manufacturer, 20.82, is a good estimate for the gain ratio, while the ratio of the low and high gain is a bit high with ~22.25.

$$S(x,y;\Theta) = \frac{A}{2\pi\sigma_x\sigma_y\sqrt{1-\rho^2}} \cdot \exp\left(-\frac{1}{\sqrt{1-\rho^2}}\right) \cdot \exp\left(-\frac{(x-\mu_x)^2}{2\cdot{\sigma_x}^2} - \frac{(y-\mu_y)^2}{2\cdot{\sigma_y}^2}\right) \cdot \exp\left(\frac{(x-\mu_x)\cdot(y-\mu_y)}{\sigma_x\cdot\sigma_y\cdot\sqrt{1-\rho^2}}\right) \quad (2)$$

with parameters $\Theta = (A, \mu_x, \mu_y, \sigma_x, \sigma_y, \rho)$, where $\mu_{(x,y)}$ and $\sigma_{(x,y)}$ denote the centroid position and standard deviation in the x and y directions, respectively, and ρ denotes the correlation parameter. Note that the double integral over the entire (x, y)-plane yields A, which is equivalent to the entire flux from the point source. Note further that, technically, the signal within each pixel would correspond to the double integral of the Gaussian over the pixel area [14]. For the purposes of this paper, this will be approximated by the value of the Gaussian at the pixel centre. In order to estimate the camera background N, we construct a master bias and master dark frame at the same exposure time from ten individual frames each and set the corresponding master as given. Lastly, the signal should be modulated by a flat field estimate, which would serve to adjust the incident flux before the digitisation process based on, e.g., vignetting effects and quantum efficiency non-uniformities. This aspect will be incorporated in future iterations of the brightness estimation process.

The observed counts n_i in each pixel $i = 1, 2, \dots, K$ are assumed to be generated from a Poisson distribution based on the total flux $I_i(\Theta)$ within each pixel,

$$\mathcal{P}(n_i; I_i(\Theta)) = \frac{\exp\left(-I_i(\Theta)\right)\cdot(I_i(\Theta))^n}{n_i!} \quad . \quad (3)$$

Assuming the signal within each pixel is independent of other pixels, the joint likelihood of observing the corresponding counts in every pixel is then the product of likelihoods of observing each pixel count n_i given the predicted flux I_i in each corresponding pixel,

$$\mathcal{L} = \prod_{i=1}^{K} \mathcal{P}(n_i; I_i(\Theta)) \quad . \quad (4)$$

Note that this likelihood implicitly assumes a fully linear detector response and no upper limit on the possible observed counts, two conditions that in practice are not fulfilled. This in turn results in poor behaviour on overexposed or saturated images.

Obtaining the brightness is then a question of obtaining a maximum likelihood estimator for A in Equation (2), which is parameterised such that it equals the integral of the Gaussian over the 2D domain and thus the total brightness assumed to be received from the object. In practice, it is numerically much more convenient and stable to minimise the negative log-likelihood instead [15], i.e., minimise

$$-\ln(\mathcal{L}) = -\sum_{i=1}^{K} \ln\left(\mathcal{P}(n_i; I_i(\Theta))\right) \quad (5)$$

$$= -\sum_{i=1}^{K} I_i(\Theta) - n_i \cdot \ln\left(I_i(\Theta)\right) + \sum_{j=1}^{n_i} \ln(j) \quad (6)$$

This method will be referred to as "Gaussian fit".

The second method is similar to the first one, however, using a scaled Moffat distribution instead of a Gaussian. The Moffat distribution is named after [16], who showed that the point-spread-function of stars could not quite accurately be described by a Gaussian profile. Since we will be dealing with unresolved objects, we expect the arguments should hold for observations of resident space objects just like for stellar observations. The parametrisation used in this paper is

$$S(x,y;\Theta) = A \cdot \frac{\beta-1}{\pi\cdot\alpha^2} \cdot \left(1 + \frac{(x-\mu_x)^2 + (y-\mu_y)^2}{\alpha^2}\right)^{-\beta} \quad (7)$$

with parameters $\Theta = (A, \mu_x, \mu_y, \alpha, \beta)$, where A again denotes the double integral of the Moffat profile over the entire detector plane, $\mu_{(x,y)}$ denote the centroid position in the x and y direction, respectively, α is the width parameter, and β denotes the profile slope parameter. Note that in this case, unlike in the Gaussian case, the distribution is inherently assumed to be rotationally symmetric, a constraint avoided in the Gaussian case in Equation (2). However, the added flexibility in the wings of the distribution may be beneficial later on. Again, the brightness is obtained via the maximum likelihood estimator for A, substituting only the model for the signal S in Equation (1) for the Moffat profile prediction. This method will be referred to as "Moffat fit".

The third method is to define a rectangular aperture with edges twice the size of the empirically set full-width at half-maximum (FWHM) obtained by the individual fit method used (Gaussian or Moffat), then sum up the ADUs for each pixel fully within this aperture. The bias and dark signal obtained from master dark frames are subtracted from each pixel, as well as the sky background. The latter is estimated as the median count of all ADUs within a small window surrounding the aperture (typically around 30×30 pixels, while the source is confined mostly to around 10×10 pixels) in the data after subtraction of the master dark and bias frame. This method assumes that most of the source flux is contained within this aperture. Consequently, it sould yield a decent approximation for the incident flux, even though it will be slightly biased to lower values due to some of the signal being excluded as it lies outside the aperture. For the remainder of this paper, this method will be referred to as "aperture summation", and the resulting brightness will be referred to as "aperture sum", with the corresponding model informing the aperture mentioned alongside it.

In order to obtain estimators for the maximum likelihood (or minimum negative log-likelihood) estimators for the parameters Θ and the background B in the Gaussian and Moffat fits, we use the sequential least squares minimisation routine within the `scipy` python package (i.e., the `scipy.optimize.minimize()` function using the `SLSQP` method), version 1.14.1 [17]. Consequently, uncertainties for brightness estimates cannot yet be provided; this will be the topic of future efforts.

5. RESULTS

5.1. 2002–040B

Comparing the brightness estimates based on the three methods introduced in section 4, we obtain the data shown in Figure 1 for the high and low gain channels (upper and lower panel, respectively). The brightness information displayed here gives the average count rate as recorded on the detector for each observation, meaning that no compensation for atmospheric effects, topocentric distance, phase angle or other effects unmentioned so far was performed. Due to the observations being performed in batches of ten as alluded to in section 3, the light curve displays clusters of observations followed by longer periods of time without data points.

Starting with the high gain observations (upper panel in Figure 1), the different methods produce similar results, albeit with differences of some tens of percent. The overall trend is an increase in brightness. The aperture sum informed by the Gaussian fit parameters (purple pluses) very closely resembles the Gaussian fit integral (black squares), increasing the credibility of both results. Interestingly, the Moffat profile returns notably different results. Not only do these results not correspond to the Gaussian fit and Gaussian informed aperture summation results, the fit integral (red diamonds) is also offset from the aperture sum (yellow crosses) informed by the fit parameters by about 25%.

This may be a result of several factors at play, from which three have been identified as likely the strongest contributors. Firstly, the estimates for the background in the image differ very little between the Gaussian fit and aperture summation. This is no longer true for the Moffat fit, where the best fit profile consistently covers a large area around the image object with a small tail, leading the background to be estimated lower than in the aperture summation or the Gaussian fit method (see the upper panel of Figure 2). This in turn leads to a much higher integral over the detector plane, explaining the increased brightness estimate from the Moffat fit relative to the Gaussian fit integral and Gaussian informed aperture sum.

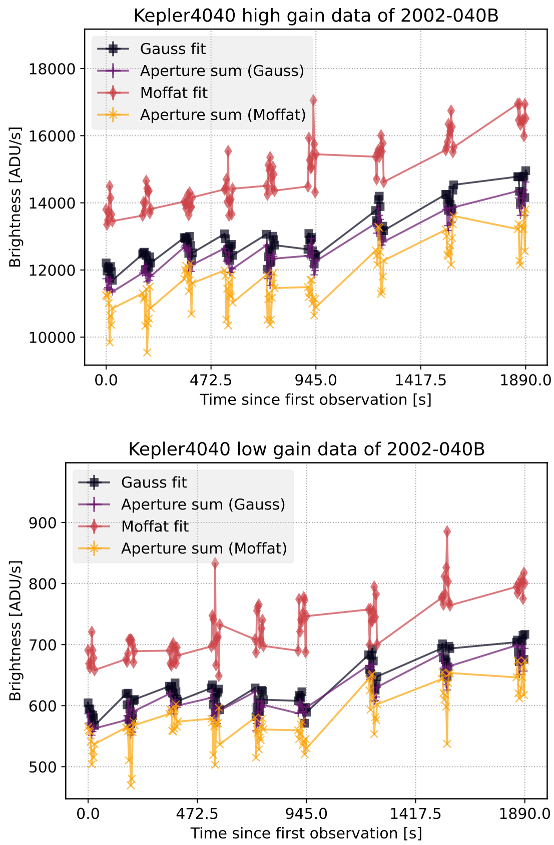

Figure 1. Light curve of 2002–040B extracted from the Kepler4040 high gain images. The black squares and red diamonds correspond to the Gauss and Moffat fits, while the purple pluses and yellow crosses correspond to the Gauss and Moffat informed aperture sums around, respectively.

Secondly, since the source was consistently located close to the field of view's edge, it tended to be elongated or distorted. While the Gaussian profile could adapt to this by adjusting the standard deviations and correlation parameters, the Moffat profile is restricted to a circular form, making it an inadequate model for the distorted objects. While not confirmed, we suspect that the asymmetric brightness distributions contribute to lowering the profile parameter β while keeping the width parameter α (see Equation (7)) pretty much constant, leading to a larger integral value A.

Lastly, the Moffat profile integral within a given pixel may be approximated insufficiently accurately by the value at the pixel center, leading to a biased likelihood estimation. This hypothesis will be investigated in the

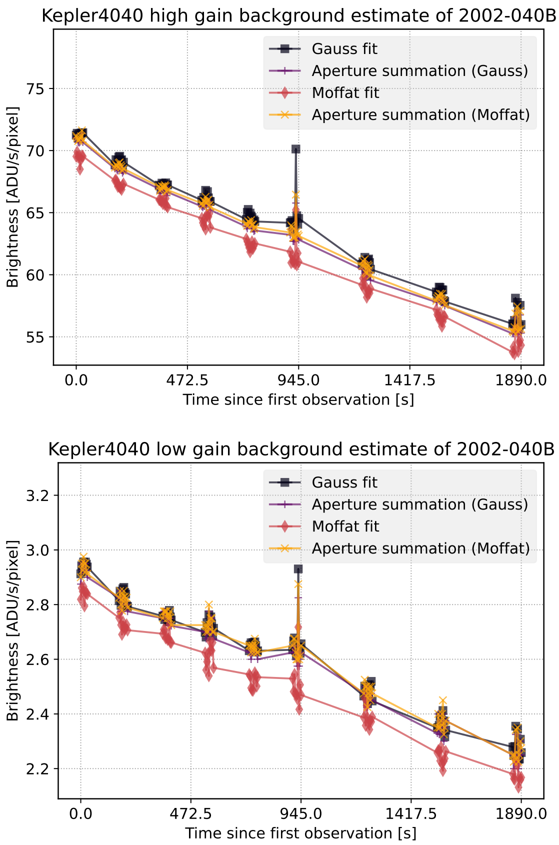

Figure 2. Estimated background for the light curves of 2002–040B extracted from the Kepler4040 high gain images. The colours and symbols are the same as in Figure 1.

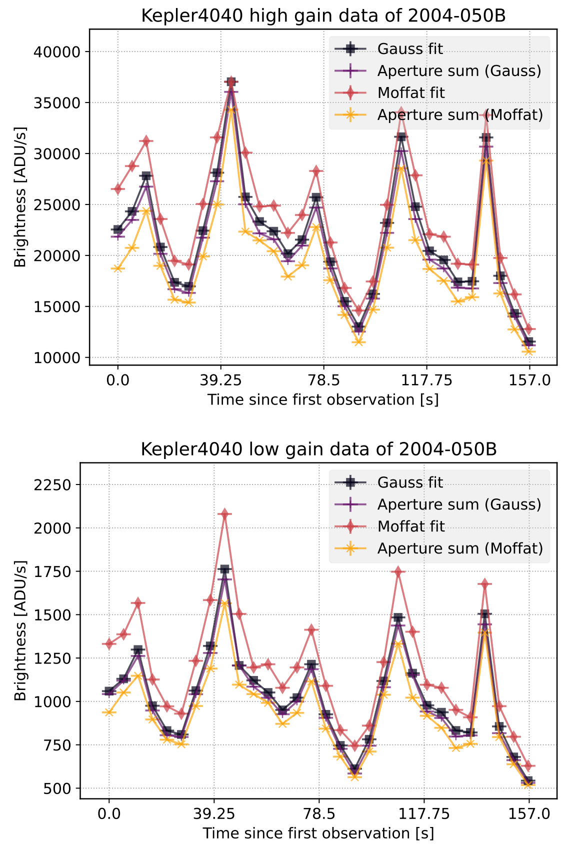

Figure 3. Light curve of 2004–050B extracted from the Kepler4040 high gain (upper panel) and low gain (lower panel) images. The colours and symbols are the same as in Figure 1.

future.

Concerning the low gain channel (Figure 1, lower panel), the same overall conclusions can be drawn, as the behaviour is largely the same as for the high gain channel. In fact, the ratio of brightnesses is consistently around $\sim$21. There are some deviations in the details, but drawing conclusions about the quality of the low and high gain estimators for in terms of accuracy at this point would be premature. Furthermore, the nature of the minimisation algorithm leads to potentially different results with different initial guesses, explaining the deviations visible at least in part.

We can also see a similar trend in the background estimate (Figure 2, lower panel) as in the high gain channel case. Again, the Moffat profile yields a lower estimate than the other methods, all of which are in very good agreement in this channel. Once again, this weakens the standpoint of the Moffat profile being a suitable model for the cases encountered in our observations and strengthens that of the Gaussian and the (Gaussian informed) aperture summation.

5.2. 2004–050B

Concerning the data of 2004–050B, Figure 3 shows the high and low gain light curves extracted from the Kepler4040 frames. As before, there is some discrepancy between the different models and methods. Interestingly, the same pattern emerges as before, with the Moffat fit yielding the highest estimates, followed by the Gauss fit. Close to that is the Gauss aperture sum, while the Moffat aperture sum yields the lowest estimates over the entire light curve. Still, outside of these method-based biases, the light curves agree well within reasonable uncertainties.

The light curves also show a very similar structure, again multiplied by a factor of $\sim$21. In this case, however, the pattern emerging clearly indicates a periodic component to the signal, which may be a hint at rotation of the object. In order to confirm or dismiss this, we performed a Lomb-Scargle analysis [18, 19]. Note that, for the calculation of Lomb-Scargle power, uncertainties on the observable are required. Since we have no estimate of the uncertainties so far, we will treat all uncertainties in brightness as being $1\,\mathrm{ADU/s}$ purely for numerical reasons. Due to the signal being well above the background

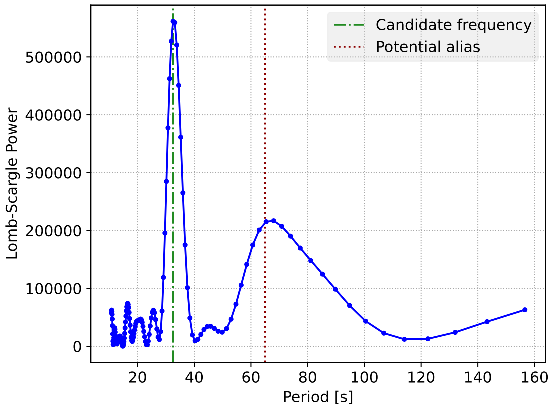

Figure 4. Lomb-Scargle periodogram of the low gain Gauss fit light curve of 2004–050B, rescaled from frequencies to periods. The blue dots indicate the test frequencies, the vertical green dash-dotted line indicates the most likely (i.e., highest power or "main") test frequency, and the dotted red line indicates half of the main frequency. Note the reduced, but still quite notable power at this location.

level in all exposures, the introduction of true uncertainties should result in mostly a scaling of the powers in absolute, but hardly in relative terms. The frequencies were chosen such that approximately 10 test frequencies should be contained within one peak, that the lowest frequency would cover half the observation window, and the highest frequency would be given by the sampling frequency. For a comprehensive overview of the Lomb-Scargle periodogram and its analysis as well as details on the approach used, we refer the interested reader to [20]. Due to the its results being the closest to an average of the four approaches used so far, we will only deal with the Gauss fit light curve for the remaining section, specifically with the low gain Gauss fit light curve. The resulting Lomb-Scargle periodogram is shown in Figure 4. There is a very prominent peak at a candidate period of $\sim$32.5 s. This frequency will now be referred to as the "main" frequency.

However, the second notable peak at half the main frequency, i.e., double the main period, is also sufficiently prominent to warrant at least curious investigation. The corresponding peak in power is located at a test frequency of $\sim$68.0 s. To see the effect of both frequencies on the light curve, the time-folded data (i.e., replacing time stamps t_i with the rotational phase $p_i = ((t_i - t_{\mathrm{ref}}) \cdot f) \bmod 1$, with reference time t_{ref}, frequency f, and the modulus operator mod) for the main and the secondary frequency are shown in the upper and lower panels of Figure 5, respectively. Note that the reference time was set to the timestamp of the first observation. At first glance, both folded light curves produce plausible results. The main frequency results in a single, prominent peak, followed by a fanning out of the brightness while it decreases to its previous level. This fanning out is, however, somewhat structured still, with what seem to be a flatter and a steeper decay overlapping. In contrast, the secondary frequency results in two maxima of somewhat different height, but with different brightness profiles following them. Here, the fanning out is much less pronounced and seems to be more an effect that affects all observations uniformly. One source of such a uniform decrease may be an increase in topological distance or in observational conditions, which have not been compensated for in this paper.

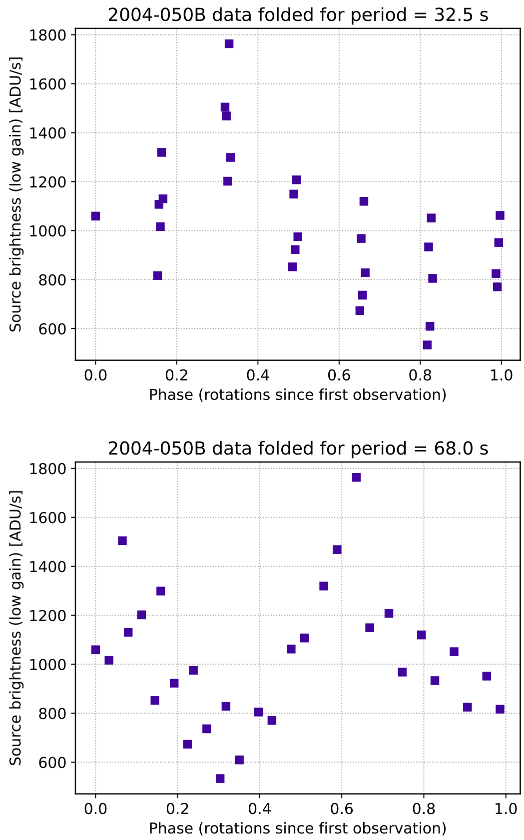

Figure 5. Low gain Gauss fit light curve of 2004–050B time-folded by the main frequency (upper panel) and the secondary frequency (lower panel) from the Lomb-Scargle periodogram (Figure 4). Integer multiples of full rotations are modulated out to see the brightness at corresponding phases within the rotation cycle. Phase 0 corresponds to the relative attitude of the first observation performed. Clearly visible is a peak at phase $\sim$0.3 for the main frequency and two peaks around $\sim$0.1 and $\sim$0.6 for the secondary frequency, respectively.

Given the shape of 2004–050B – a Delta IV upper stage rocket body – and the somewhat cylindrical nature of its tank section, one would expect to see two maxima and possibly somewhat different brightness drops after the maxima within a single rotation perpendicular to its axis of symmetry. Given this context, we conclude the secondary rotation frequency to be the true rotation frequency.

Deriving uncertainties directly from the Lomb-Scargle power is not without issues (see [20], section 7.4 for a concise overview). However, since in this case all observations are virtually equidistant in time and the peaks are sufficiently well separated, we will adopt a rough uncertainty estimate based on the distance to the next-nearest test frequencies. Note that this choice is somewhat arbitrary and made to ensure that the Lomb-Scargle power has dropped below the peak height. As a result, we obtain a synodic rotational period of (68.0 ± 5.5) s. This period is consistent with the value listed in the Space Debris Light Curve Database [7] for October 2021, which lists a value of (64.263 ± 0.004) s obtained from a total of 499 brightness measurements. The large discrepancy in uncertainties is explainable by the rough estimation method on our side, the more sophisticated approach on the side of [7], and the vastly different amounts of observations used (30 versus 499).

6. CONCLUSION

We have demonstrated the ability of our SMART-03-ELSA station to obtain light curves of resident space objects. We compared three different methods of obtaining brightness estimations and showed that, at least in the context resident space objects tracked at the edges of the field of view and potentially imperfectly, the Moffat profile may not be a suitable model for the distribution of light on the sensor. We further showed that, within the same context, modelling the light distribution as a 2-dimensional Gaussian with non-zero correlation and using the integral as an estimator for the brightness shows negligible differences to simple summation over a sufficiently large aperture. Of course, this can change in the context of saturated images, where a well-defined model can still infer brightnesses that partially saturate the image. Further, an extension of the Moffat profile accounting for asymmetry and correlation, similar to the Gaussian profile used in this paper, may be conceivable, the performance of which would be up for investigation in the future.

This work made use of the following software packages: `astropy` [21, 22, 23], `Jupyter` [24, 25], `matplotlib` [26], `numpy` [27], `python` [28], and `scipy` [17, 29]. This research has made use of NASA's Astrophysics Data System. Software citation information aggregated using `The Software Citation Station` [30, 31].

REFERENCES

1. https://www.space-track.org/, retrieved March 7th, 2025.

2. Šilha, J. and Zigo, M., Hrobár, T., Jevčák, P., Verešvárska, M., (2021). Light curves application to space debris characterization and classification. In *Proc. 8th European Conference on Space Debris*, p. 116.

3. Koshkin, N., Shakun, L., Kozhukhov, O., Kozhukhov, D., Mamarev, V., Prysiaznyi, V., Ozeryan, A., Bilinsky, A., Kudak, V., Neubauer, I., (2021). Simultaneous multi-site photometry of LEO satellites for rotation characterization. In *Proc. 8th European Conference on Space Debris*, p. 40.

4. Šilha, J., Hrobár, T., Zigo, M., Sabolová, K., Kyselica, D., (2023). Space Debris Rotation Properties and Characterization Using Rotation Phase Curves Extracted from Public Photometric Catalogues. In *Proc. 2nd International Orbital Debris Conference*, Vol. 2852, p. 6028.

5. Kerr, E., Falco, G., Maric, N., Petit, D., Talon, P., Petersen, E. G., Dorn, C., Eves, S., Sánchez-Ortiz, N., Gonzalez, R. D., Nomen-Torres, J., (2021). Light Curves for GEO object characterisation. In *Proc. 8th European Conference on Space Debris*, p. 49.

6. Kobayashi, D., Frueh., C., (2024). Image Recovery from Low Earth Orbit by Leveraging Turbulence and Light Curves, *Journal of Guidance Control Dynamics*, **47**(4), 623–637

7. Šilha, J., Krajčovič, S., Zigo, M., Tóth, J., Žilková, D., Zigo, P., Kornoš, L., Šimon, J., Schildknecht, T., Cordelli, E., Vananti, A., Mann, H. K., Rachman, A., Paccolat, C., Flohrer, T., (2020). Space debris observations with the Slovak AGO70 telescope: Astrometry and light curves, *Advances in Space Research*, **65**(8), 2018–2035

8. Šilha, J., Schildknecht, T., Pittet, J. N., Rachman, A., Hamara, M., (2017). Extensive light curve database of Astronomical Institute of he University of Bern. In *Proc. 7th European Conference on Space Debris*, p. 234.

9. Fiedler, H., Herzog, J., Hofmann, B., Kahle, R., Meinel, M., Prohaska, M., Rack, K., Schildknecht, T., Siggel, M., Stoffers, M., Kurnatowski, L., Wasser, Y., Weigel, M., (2019). SMARTnet™and BACARDI. In *Proc. 70th International Astronautical Congress*, IAF.

10. Fiedler, H., Bergmann, C. M., Griese, F., Herzog, J., Hofmann, B., Kleint, L., Meinel, M., Prohaska, M., Rack, K., Schildknecht, T., Schlepp, B., Schmitz, S., Stoffers, M., Zollo, A., (2023). Five Years of SMARTnet: Data, Processing, and Improvements. In *Proc. 2nd ESA NEO and Debris Detection Conference*, ESA, p. 85.

11. Herzog, J., Hofmann, B., Fiedler, H., Prohaska, M., Schildknecht, T., (2021). Software and Hardware to Improve a Remote Telescope Station. In *Proc. 8th European Conference on Space Debris*, p.13.

12. Ascanio Hecker, Y., Rosok, R., Bergmann, C. M., Herzog, J., Fiedler, H., (2024). Impact of a Rolling Shutter on Light Curves of Resident Space Objects in High Altitude Orbits. In *Proc. 22nd IAA Symposium on Space Debris*, pp 2001–2012

13. Bergmann, C. M., Herzog, J., Hoffmann, B., Prohaska, M., Ascanio Hecker, Y., Fiedler, H., Schild-

knecht, T., Kleint, L., submitted. SMARTies – a software suite for flexible and fully automated control of multi-sensor telescope stations.

14. Vicuña, M. L., Silva, J. F., Mendez, R. A., Orchard, M. E., Espinosa, S., Tregloan-Reed, J., (2024). Optimal Photometry of Point Sources: Joint Source Flux and Background Determination on Array Detectors-from Theory to Practical Implementation, *Publications of the Astronomical Society of the Pacific*, **136**(1), 014501
15. Piech, C., (2023). Log Probabilities. In *Probability for Computer Scientists*, Version 0.923, Department of Computer Science, Stanford University, USA. Online: https://chrispiech.github.io/probabilityForComputerScientists/en/index.html (last visited March 12th, 2025).
16. Moffat, A. F. J., (1969). A Theoretical Investigation of Focal Stellar Images in the Photographic Emulsion and Application to Photographic Photometry, *Astronomy and Astrophysics*, **3**, 455
17. Gommers, R., Virtanen, P., Hamberland, M., Burovski, E., Weckesser, W., Reddy, T., Oliphant, T. E., Cournapeau, D., Nelson, A., alexbrc, Roy, P., Peterson, P., Polat, I., Wilson, J., endolith, Mayorov, N., van der Walt, S., Brett, M., Laxalde, D., Larson, E., Sakai, A., Millman, J., Colley, L., Lars, peterbell10, Carey, C. J., van Mulbregt, P., Bowhay, J., eric-jones, Striega, K., (2024). *scipy/scipy: SciPy 1.14.1*, Zenodo.
18. Lomb, N. R., (1976). Least-Squares Frequency Analysis of Unequally Spaced Data, *Astropysics and Space Science*, **39**(2), 447–462
19. Scargle, J. D., (1982). Studies in astronomical time series analysis. II. Statistical aspects of spectral analysis of unevenly spaced data., *Astrophysical Journal*, **263**, 835–853
20. VanderPlas, J. T., (2018). Understanding the Lomg-Scargle Periodogram, *The Astrophysical Journal Supplement Series*, **236**(1), 16
21. Astropy Collaboration, Robitaille, T. P., Tollerud, E. J., Greenfield, P., Droettboom, M., Bray, E., Aldcroft, T., Davis, M., Ginsburg, A., Price-Whelan, A. M., Kerzendorf, W. E., Conley, A., Crighton, N., Barbary, K., Muna, D., Ferguson, H., Grollier, F., Parikh, M. M., Nair, P. H., Unther, H. M., Deil, C., Woillez, J., Conseil, S., Kramer, R., Turner, J. E. H., Singer, L., Fox, R., Weaver, B. A., Zabalza, V., Edwards, Z. I., Azalee Bostroem, K., Burke, D. J., Casey, A. R., Crawford, S. M., Dencheva, N., Ely, J., Jenness, T., Labrie, K., Lim, P. L., Pierfederici, F., Pontzen, A., Ptak, A., Refsdal, B., Servillat, M., Streicher, O., (2013). Astropy: A community Python package for astronomy, *Astronomy & Astrophysics*, **558**, A33
22. Astropy Collaboration, Price-Whelan, A. M., Sipőcz, B. M., Günther, H. M., Lim, P. L., Crawford, S. M., Conseil, S., Shupe, D. L., Craig, M. W., Dencheva, N., Ginsburg, A., VanderPlas, J. T., Bradley, L. D., Pérez-Suárez, D., de Val-Borro, M., Aldcroft, T. L., Cruz, K. L., Robitaille, T. P., Tollerud, E. J., Ardelean, C., Babej, T., Bach, Y. P., Bachetti, M., Bakanov, A. V., Bamford, S. P., Barentsen, G., Barmby, P., Baumbach, A., Berry, K. L., Biscani, F., Boquien, M., Bostroem, K. A., Bouma, L. G., Brammer, G. B., Bray, E. M., Breytenbach, H., Buddelmeijer, H., Burke, D. J., Calderone, G., Cano Rodríguez, J. L., Cara, M., Cardoso, J. V. M., Cheedella, S., Copin, Y., Corrales, L., Crichton, D., D'Avella, D., Deil, C., Depagne, É., Dietrich, J. P., Donath, A., Droettboom, M., Earl, N., Erben, T., Fabbro, S., Ferreira, L. A., Finethy, T., Fox, R. T., Garrison, L. H., Gibbons, S. L. J., Goldstein, D. A., Gommers, R., Greco, J. P., Greenfield, P., Groener, A. M., Grollier, F., Hagen, A., Hirst, P., Homeier, D., Horton, A. J., Hosseinzadeh, G., Hu, L., Hunkeler, J. S., Ivezić, Ž., Jain, A., Jenness, T., Kanarek, G., Kendrew, S., Kern, N. S., Kerzendorf, W. E., Khvalko, A., King, J., Kirkby, D., Kulkarni, A. M., Kumar, A., Lee, A., Lenz, D., Littlefair, S. P., Ma, Z., Macleod, D. M., Mastropietro, M., McCully, C., Montagnac, S., Morris, B. M., Mueller, M., Mumford, S. J., Muna, D., Murphy, N. A., Nelson, S., Nguyen, G. H., Ninan, J. P., Nöthe, M., Ogaz, S., Oh, S., Parejko, J. K., Parley, N., Pascual, S., Patil, R., Patil, A. A., Plunkett, A. L., Prochaska, J. X., Rastogi, T., Reddy Janga, V., Sabater, J., Sakurikar, P., Seifert, M., Sherbert, L. E., Sherwood-Taylor, H., Shih, A. Y., Sick, J., Silbiger, M. T., Singanamalla, S., Singer, L. P., Sladen, P. H., Sooley, K. A., Sornarajah, S., Streicher, O., Teuben, P., Thomas, S. W., Tremblay, G. R., Turner, J. E. H., Terrón, V., van Kerkwijk, M. H., de la Vega, A., Watkins, L. L., Weaver, B. A., Whitmore, J. B., Woillez, J., Zabalza, V., Astropy Contributors, (2018). The Astropy Project: Building an Open-science Project and Status of the v2.0 Core Package, *The Astronomical Journal*, **156**(3), 123
23. Astropy Collaboration, Price-Whelan, A. M., Lim, P. L., Earl, N., Starkman, N., Bradley, L., Shupe, D. L., Patil, A. A., Corrales, L., Brasseur, C. E., Nöthe, M., Donath, A., Tollerud, E., Morris, B. M., Ginsburg, A., Vaher, E., Weaver, B. A., Tocknell, J., Jamieson, W., van Kerkwijk, M. H., Robitaille, T. P., Merry, B., Bachetti, M., Günther, H. M., Aldcroft, T. L., Alvarado-Montes, J. A., Archibald, A. M., B'odi, A., Bapat, S., Barentsen, G., Baz'an, J., Biswas, M., Boquien, M., Burke, D. J., Cara, D., Cara, M., Conroy, K. E., Conseil, S., Craig, M. W., Cross, R. M., Cruz, K. L., D'Eugenio, F., Dencheva, N., Devillepoix, H. A. R., Dietrich, J. P., Eigenbrot, A. D., Erben, T., Ferreira, L., Foreman-Mackey, D., Fox, R., Freij, N., Garg, S., Geda, R., Glattly, L., Gondhalekar, Y., Gordon, K. D., Grant, D., Greenfield, P., Groener, A. M., Guest, S., Gurovich, S., Handberg, R., Hart, A., Hatfield-Dodds, Z., Homeier, D., Hosseinzadeh, G., Jenness, T., Jones, C. K., Joseph, P., Kalmbach, J. B., Karamehmetoglu, E., Kaluszy'nski, M., Kelley, M. S. P., Kern, N., Kerzendorf, W. E., Koch, E. W., Kulumani, S., Lee, A., Ly, C., Ma, Z., MacBride, C., Maljaars, J. M., Muna, D., Murphy, N. A., Norman, H., O'Steen, R., Oman, K. A., Pacifici, C., Pascual, S., Pascual-Granado, J., Patil, R. R., Perren, G. I., Pickering, T. E., Rastogi, T., Roulston, B. R., Ryan, D. F., Rykoff, E. S., Sabater, J., Sakurikar, P., Salgado, J., Sanghi, A., Saunders, N., Savchenko, V., Schwardt, L., Seifert-Eckert, M.,

Shih, A. Y., Jain, A. S., Shukla, G., Sick, J., Simpson, C., Singanamalla, S., Singer, L. P., Singhal, J., Sinha, M., SipHocz, B. M., Spitler, L. R., Stansby, D., Streicher, O., Šumak, J., Swinbank, J. D., Taranu, D. S., Tewary, N., Tremblay, G. R., de Val-Borro, M., Van Kooten, S. J., Vasovi'c, Z., Verma, S., de Miranda Cardoso, J. V., Williams, P. K. G., Wilson, T. J., Winkel, B., Wood-Vasey, W. M., Xue, R., Yoachim, P., Zhang, C., Zonca, A., Astropy Project Contributors, (2022). The Astropy Project: Sustaining and Growing a Community-oriented Open-source Project and the Latest Major Release (v5.0) of the Core Package, *The Astrophysical Journal*, **935**(2), 167

24. Perez, F., Granger, B. E., (2007). IPython: A System for Interactive Scientific Computing, *Computing in Science and Engineering*, **9**(3), 21-29

25. Kluyver, T., Ragan-Kelley, B., Pérez, F., Granger, B., Bussonnier, M., Frederic, J., Kelley, K., Hamrick, J., Grout, J., Corlay, S., Ivanov, P., Avila, D., Abdalla, S., Willing, C., (2016). Jupyter Notebooks – a publishing format for reproducible computational workflows. In *Positioning and Power in Academic Publishing: Players, Agents and Agendas* (Eds. F. Loizides & B. Schmidt), IOS Press, pp 87–90

26. Hunter, J. D., (2007). Matplotlib: A 2D graphics environment, *Computing in Science & Engineering*, **9**(3), 90–95

27. Harris, C. R., Millman, K. J., van der Walt, S. J., Gommers, R., Virtanen, P., Cournapeau, D., Wieser, E., Taylor, J., Berg, S., Smith, N. J., Kern, R., Picus, M., Hoyer, S., van Kerkwijk, M. H., Brett, M., Haldane, A., Fernández del Río, J., Wiebe, M., Peterson, P., Gérard-Marchant, P., Sheppard, K., Reddy, T., Weckesser, W., Abbasi, H., Gohlke, C., Oliphant, T. E., (2020). Array programming with NumPy, *Nature*, **585**(7825), 357–362

28. van Rossum, G., Drake, F. L., (2009). *Python 3 Reference Manual*, CreateSpace, Scotts Valley, California, USA.

29. Virtanen, P., Gommers, R., Oliphant, T. E., Haberland, M., Reddy, T., Cournapeau, D., Burovski, E., Peterson, P., Weckesser, W., Bright, J., van der Walt, S. J., Brett, M., Wilson, J., Millman, K. J., Mayorov, N., Nelson, A. R. J., Jones, E., Kern, R., Larson, E., Carey, C. J., Polat, İ, Feng, Y., Moore, E. W., VanderPlas, J., Laxalde, D., Perktold, J., Cimrman, R., Henriksen, I., Quintero, E. A., Harris, C. R., Archibald, A. M., Ribeiro, A. H., Pedregosa, F., van Mulbregt, P., SciPy 1.0 Contributors, (2020). SciPy 1.0: Fundamental Algorithms for Scientific Computing in Python, *Nature Methods*, **17**, 261–272

30. Wagg, T., Broekgaarden, F. S., (2024). Streamlining and standardizing software citations with The Software Citation Station, *arXiv e-prints*, arXiv:2406.04405

31. Wagg, T., Broekgaarden, F. S., Gültekin, K., (2024). *TomWagg/software-citation-station: v1.2*, Zenodo